Unveiling the effect of the electrodes area on the corrosion mechanism of a graphite - AA2024-T3 galvanic couple by localised electrochemistry

L.B. Coelho [a, *], M. Taryba [b], M. Alves [b], M.F. Montemor [b], M.-G. Olivier [a, c]

[a] *Materials Science Department, Faculty of Engineering, University of Mons, 20 Place du Parc, 7000 Mons, Belgium*
[b] *Centro de Quimica Estrutural, Departamento de Engenharia Quimica, Instituto Superior Técnico, Universidade de Lisboa, Av. Rovisco Pais, 1049-001 Lisboa, Portugal*
[c] *Materia Nova Asbl, Avenue Copernic 1, 7000 Mons, Belgium*

ARTICLE INFO

ABSTRACT

The corrosion mechanism of two AA2024-T3/graphite galvanic couples, with different electrodes area ratio, was studied in 12.00 mM NaCl solution using the Scanning Vibrating Electrode Technique (SVET) and the Scanning Ion-Selective Electrode Technique (SIET). Both techniques were used, quasi-simultaneously, to monitor the current density distribution and the pH associated to the corrosion process occurring in the galvanic couples. The morphological features and the elemental composition of the electrodes' surfaces, after 20 h of immersion, were analysed by Scanning Electron microscopy and Energy Dispersive X-ray Spectroscopy (SEM-EDX). The results show that the area of the electrodes in the galvanic couple significantly influences the corrosion mechanism. For the couple, with the highest AA2024/graphite area ratio (M1), both anodic and cathodic processes developed on the alloy surface, resulting in localised corrosion (trenching of the matrix around intermetallics) at the cathodic zones as detected by SVET and SIET. A more generalised anodic dissolution of AA2024 (corrosion of the matrix and grain boundaries) was observed for the sample with the lowest area ratio (M2), however.

© 2018 Elsevier Ltd. All rights reserved.

1. Introduction

The use of composite materials in structural components of aircrafts has been progressively increasing to allow weight reduction and to meet the actual energy saving policies [1–3]. The use of Carbon Fibre-Reinforced Polymers (CFRP) creates multi-material junctions that often comprise aluminium alloys [4,5]. These alloys represent around 20 wt% in modern aircraft designs [6]. Moreover, metallic rivets responsible for assembling the composite parts with the Al alloys panels (particularly the AA2024) create an electrical contact between these dissimilar materials. Therefore, since CFRP is much nobler than AA2024, galvanic corrosion is very likely [4,7,8]. Furthermore, the favourable oxygen reduction reaction (ORR) kinetics on graphite are expected to promote the corrosion of the alloy as well [9]. Thus, the understanding of the galvanic corrosion problems between AA2024 and CFRP is a crucial issue towards

implementation of efficient corrosion protection strategies, allowing the wider use of these materials in aeronautical applications.

It is well known that the AA2024 alloy is very susceptible to corrosion in NaCl electrolyte due to its heterogeneous microstructure and presence of inclusions [10–12]. Intermetallic particles (IMPs), such as the Al-Cu and Al-Cu-(Fe,Mn)-containing phases, act as cathodic sites relatively to the Al matrix and can support the ORR [11,13,14]. On the other hand, the most abundant intermetallic phase of AA2024, the S-phase (Al_2CuMg), represents ca. 60% of the precipitates [10] and is less noble than the Al matrix, evidencing anodic behaviour at the early stage of corrosion [11,15]. The corrosion mechanism involves a self-dissolution step (selective dissolution of Al and Mg [16–18]), the S-phase particles becomes progressively richer in Cu and its electrochemical behaviour turns to be more and more cathodic [10,11,14,19]. Therefore, as corrosion proceeds, the overall cathodic nature of the Cu-rich precipitates is responsible for the localised attack of the neighbour passive Al matrix. Some authors have explained that the trenching of the matrix mainly proceeds by an electrochemical mechanism (anodic dissolution of Al) [11,20]; however, others [15,21–23] consider that

the process is mainly governed by a chemical dissolution process induced by the alkaline environment surrounding the IMPs (cathodic attack). In any case, a secondary effect of the cathodic activity of the remnants is the reduction of Cu ions dissolved in solution over (and around) them, leading to nodular and uneven Cu deposits [10,19,22,23].

Recently, spatially-resolved electrochemical techniques have been able to successfully extract useful information on the corrosion and corrosion inhibition processes at the micro-scale level. In particular, Lamaka and co-workers [24] have combined the Scanning Vibrating Electrode Technique (SVET) with the Scanning Ion-Selective Electrode Technique (SIET, or micro-potentiometry) to quasi-simultaneously assess the local distributions of ionic current density and H^+ over a corroding surface. Since this pioneering work, the use of SVET/SIET quasi-simultaneously has emerged as a powerful tool to comprehend the electrochemical/chemical reactions governing the corrosion mechanism of various systems [25–31].

In the present investigation, SVET and SIET were quasi-simultaneously applied to measure, respectively, the current density and pH distributions associated with the corrosion activity on AA2024/graphite galvanic couples. A graphite foil was used to simulate the cathodic behaviour of the CFRP material (the cathodic response of carbon fibre-based composites in NaCl solution is coincident to that of pure graphite [4,32]). As demonstrated by Bellucci et al. for the galvanic couple Al alloys/GECM (Graphite-Epoxy Composite Materials) [33], the corrosion intensity of the galvanic process depended upon the cathodic area and rate of the corresponding ORR. Therefore, in this work, two different model couples (M1 and M2) having alloy/graphite area ratios of 10 and 1.5, respectively, were assembled and the corrosion process was studied in the 12.00 mM NaCl.

2. Materials and methods

2.1. AA2024/graphite galvanic coupling models

Two model galvanic couples made of AA2024 and graphite were assembled to simulate the galvanic corrosion processes occurring at the AA2024/CFRP interface. The composition by weight of the AA2024-T3 plate (supplied by Q-Lab) was: 4.65% Cu, 1.87% Mg, 0.61% Mn, 0.19% Fe, 0.13% Zn (Si, Cr and Ti < 0.02%), balance Al. This composition was determined by X-ray fluorescence (S1 TURBO$_{SD}$, Bruker) and represents the average of triplicate measurements. The 1 mm thick AA2024-T3 plate was cut into ~2 mm coupons using a lever guillotine. A few coupons were kept as such, while others were abraded using a drill tool set (Dremel) until obtaining ~0.85 mm diameter rods. Then, these AA2024 rods were cleaned by acetone and ethanol using ultrasonic bath.

The samples were mounted into an epoxy resin mould and consisted on a 0.13 mm thick graphite foil (99.8% pure, Alfa Aesar) in parallel either to the alloy coupon (M1) or to the alloy rod (M2). The graphite foils employed were ~1.5 mm and ~3 mm wide for M1 and M2, respectively. In both cases, the gap of ~1 mm between the two materials (which were not in physical contact) was respected — Fig. 1. The electrical connections were made at the back side of the epoxy holders by means of a graphite conductive adhesive (Alfa Aesar). Prior to the measurements, the analysed surfaces were ground using SiC paper (up to the 4000 grade) followed by ethanol rinse and distilled water washing and then dried with compressed air. The final ratios between the area of AA2024 and that of graphite were 10 and 1.5, respectively for M1 and M2.

2.2. SVET/SIET measurements

To investigate localised processes over the model couples, SVET and micro-potentiometry (SIET) were employed. The equipment and corresponding software were supplied by Applicable Electronics™ and Science Wares™, respectively. SVET/SIET measurements were performed quasi-simultaneously using the procedure described elsewhere [24].

Insulated Pt-Ir probes (MicroProbes™) with a platinum black deposited on the probe tip were employed as microelectrodes for SVET measurements. The probe was vibrated in two perpendicular planes, vertical (Z) and horizontal (X), at frequencies of 124 Hz (Z) and 325 Hz (X), respectively. The probe diameter was 16 μm, the amplitude of vibration was 32 μm (peak to peak) and it was positioned 100 ± 3 μm above the sample surface. Only the data obtained in the vertical plane of vibration (Z) were considered for further analysis.

For the SIET pH measurements, glass capillary micro-electrodes with a tip orifice diameter of 1.8 ± 0.2 μm were used. A pH selective ionophore-based membrane, with extended pH working range, specially developed for corrosion applications, was used [24]. The local pH selective electrode was placed 50 ± 5 μm above the surface. A homemade Ag/AgCl/0.05 M NaCl mini-electrode was used as external reference electrode. Commercial buffer solutions were used for calibration. The Nernstian slope was -56.3 ± 0.5 mV/pH. The reference potential was recorded in the bulk electrolyte before and after each measurement to detect possible potential drifts.

Accurate positioning of pH microelectrode and SVET microprobe was performed using manual micro-manipulators. Both, current density and pH, were recorded on a 36×26 (sample M1) and 31×21 (sample M2) grid in 0.012 M NaCl solution. This solution was chosen for a sake of comparison with previous results obtained with similar galvanic coupling models [34]. Corresponding distributions were recorded every hour. The scanned area was about 3.5 mm × 4.6 mm. Every measurement was performed in triplicate and their reproducibility was attested.

2.3. SEM-EDX analysis

The scanning electron microscopy experiments and the EDX analysis were performed using a Hitachi S2400 at an accelerating voltage of 20 keV or a JEOL 7001F FEG-SEM/EDX at an accelerating voltage of 15 keV. The EDX detector attached to the SEM Hitachi S2400 is a light elements detector, by Bruker (former Rontec, Germany). It is a SDD detector, model XFlash 5010. The EDX detector from the FEG-SEM is a light elements detector, by Oxford (England) model INCA 250. The reproducibility and repeatability were verified for the micrographs here presented.

2.4. Potentiodynamic polarisation curves

Potentiodynamic polarisation measurements were separately performed on a AA2024-T3 (~1 cm^2) and on a graphite foil (~7 cm^2) in 12.00 mM NaCl solution using an AMETEK Parstat 2273 (Powersuite® software). One coupon of the same alloy plate (Q-lab) employed for the construction of the models was mounted in epoxy resin and its surface was ground with SiC paper (up to the 4000 grade) prior to testing. The electrochemical set-up of the cell comprised either AA2024 or graphite as working electrode, a platinum wire as counter electrode and an Ag/AgCl/KCl$_{sat}$ (+197 mV/SHE) as reference electrode. Both anodic and cathodic polarisation curves were acquired at a scan rate of 0.1 mV s^{-1}, starting from OCP, under aerated conditions. Before starting polarisation tests, it was verified that stable OCP potentials have been reached, which generally took about 40 min. Measurements were repeated
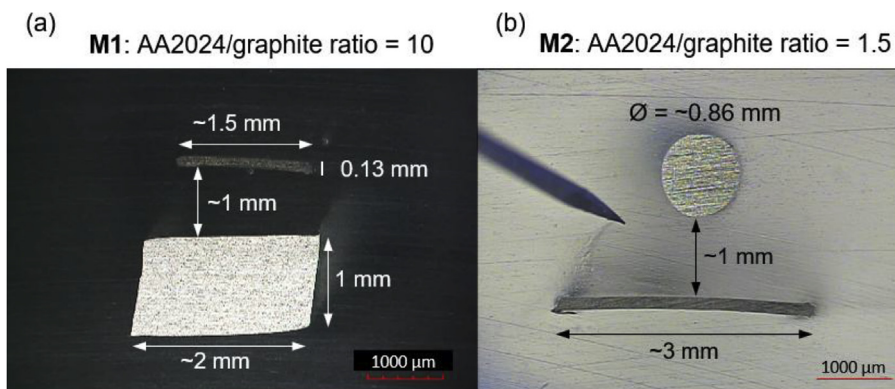
Fig. 1. Picture of the polished AA2024/graphite galvanic couples: (a) M1 and (b) M2.

at least two times.

3. Results and discussion

3.1. Corrosion behaviour of the M1 model couple

Fig. 2 presents the results of quasi-simultaneous SVET/SIET measurements obtained after 1 h, 3 h and 5 h of immersion in the NaCl electrolyte. The SVET maps highlight that cathodic activity took place on the graphite electrode, while both anodic and cathodic activities could be detected on the AA2024 alloy surface. Intense anodic activity, as expected for localised attack, was measured at the top-right sides, while slight less intense cathodic current densities were mainly detected on the bottom-left region. The SIET maps corroborate the results of SVET measurements, since the anodic and cathodic processes are clearly associated with zones of acidification and alkalinisation, respectively. At early stages of immersion, slight acidification to pH 5.2 (Fig. 2(d)) was observed over the anodic zones due to aluminium dissolution and consequent hydrolysis of the aluminium cations. Increasing acidification can be correlated to increased aluminium dissolution rate. On the other hand, the alkalinisation effects were highlighted by pH values

reaching 9.1 at the graphite electrode.

After slightly longer immersion time (~3 h of immersion), cathodic activity extended to other areas of the alloy, while its intensity decreased on the graphite surface (Fig. 2(b)). The SIET maps reflect these evolutions, evidencing slightly lower pH values over the graphite and increased pH values in the cathodic areas over the alloy (Fig. 2(e)). At this time, the anodic activity remained in a well-defined area, close to the up-right corner of AA2024, attaining a maximum current density of approximately $300\,\mu A\,cm^{-2}$ that shifted pH down to 4.5. Between 4 h and 5 h of immersion (Fig. 2(c)), the anodic sites remained active, but the magnitude of the current densities was considerably lower over graphite. The cathodic activity on the alloy presented values in the same order of magnitude of the cathodic activity on the graphite.

An optical micrograph of the alloy surface, taken *in situ* after 5 h (Fig. 2(f)), allows identifying, by simple eye inspection, areas where localised corrosion attack occurred at the zones displaying cathodic activity in the SVET maps and alkaline pH values in the SIET maps.

The increased local pH on AA2024 could be explained by the hydrogen reduction associated to fast Mg dissolution from the Mg-rich intermetallic particles, the S-phase [35]. Similarly, the generation of OH^{-} could be linked to the high self-dissolution activity of
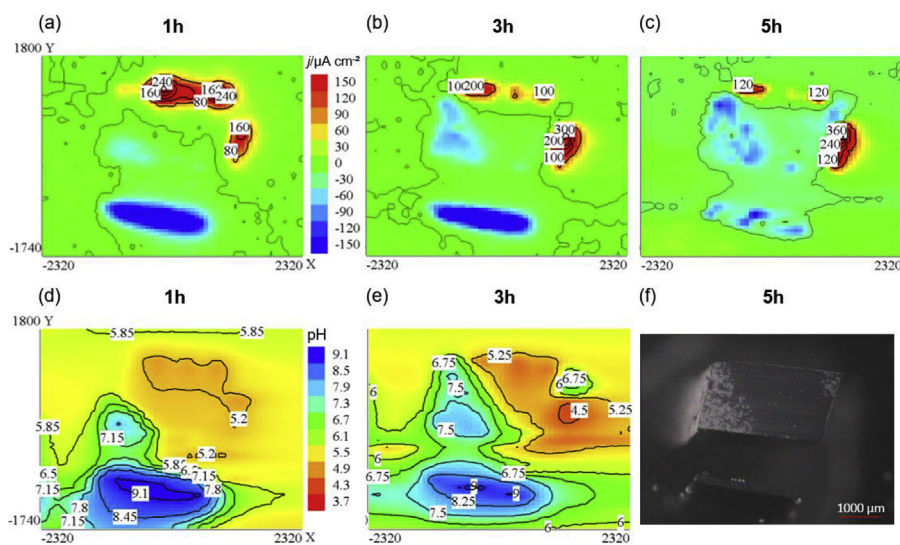

Fig. 2. (a, b, c) Current density (j / $\mu A\,cm^{-2}$) and (d, e) pH maps obtained for the M1 model couple in 12.00 mM NaCl solution after: (a, d) 1 h, (b, e) 3 h and (c) 5 h of exposure. (f) Optical micrograph of the M1 surface taken *in situ* after 5 h. X and Y coordinates represent the length of the mapping in μm. The current density and pH scales are valid for all respective j and pH maps. X and Y scales from (a) are valid for all maps. Estimated potential of M1 = −420 mV $_{(Ag/AgCl)}$ (Fig. 8).

the S-phase, as proposed by Shi et al. [27] to explain the corrosion activity of an Al/Al2CuMg model couple. Although Mg dissolution from the S-phase is very fast, occurring at the very early instants of immersion [21,36], it was possible to observe an increasing number of corroding sites with a typical geometry (grooves containing remnant in the centre) along the immersion time.

Therefore, the continuous evolution of the cathodic activity and corresponding alkalinisation process at the same locations of the AA2024 surface is probably related to ORR occurring on the Cu-rich IMPs (hydrogen evolution is not likely to occur on Cu-based cathodes due to the very high overpotential of the reaction [37]). Intermetallics able to support ORR include precipitates with permanent cathodic behaviour and Cu-rich remnants originated from the intense self-dissolution of the S-phase [10,27].

After 20 h of immersion in the NaCl electrolyte, SEM-EDX analysis was carried out. Fig. 3(a) shows a SEM micrograph of the alloy taken from a zone that presented cathodic activity. Deep trenches could be observed at the matrix/particles interface. The trenching processes are well emphasized for all types of particles found in the cathodic areas and could be attributed to the anodic dissolution of the Al matrix [15]. It is worth noting that the microcracks adjacent to these trenches are quite critical, as they constitute weaker areas for localised corrosion onset and propagation.

EDX elemental mapping underlined the presence of Cu-rich particles at the centre of the grooves (Fig. 3(c)). As it is well known, Al-Cu-Fe-Mn inclusions on the AA2024-T3 surface are efficient support for ORR, driving corrosion reactions on the adjacent matrix [11]. This effect is often assigned to local pH increase in their proximity, which in turn causes the alkaline attack of the matrix [22].

Regarding the S-phase, based on the Shi et al. investigation [27], the trenching of Al matrix around the Al2CuMg particles occurs mainly as a result of its self-dissolution, which produces significant amount of OH−. Dealloying of the S-phase, followed by the preferential dissolution of Al around the particle, is a process that

develops at the very early stages of immersion in NaCl [21]. Local Cu-enrichment around the remnants also contribute to the propagation of trenches [16]. In fact, Fig. 3 displays the absence of Mg over the small and circular particles (probably the original S-phase) and signs of Cu redeposition in the trenches around them (indicated by the white arrows). This Cu redeposition phenomenon is often triggered by the detachment of Cu-rich remnants. Furthermore, Cu-enrichment could be detected in case of the bigger Cu-rich particles shown in Fig. 3(g), as indicated by the elemental analysis performed in their centres (points 1 and 2). Indeed, intermetallics with cathodic behaviour are known to drive the reduction of copper ions dissolved in solution, leading to nodular Cu deposits [19].

Initially, the trenching of the Al matrix did not seem to be caused by anodic dissolution as result of micro-galvanic couplings with cathodic IMPs, since neither SVET nor SIET were able to monitor any sign of anodic activity on the trenched areas. Thus, the trenching might seem to have been exclusively induced by cathodic driven corrosion attack. In fact, it has been reported that Cu-containing IMPs could serve as local cathodes even when the alloy is anodically polarised [38]. In this case, the OH− ions produced by ORR taking place on the intermetallics locally increase the pH, inducing the chemical dissolution of the surrounding passive layer. According to Boag et al. [21], a pH of 9.5 is high enough to induce dissolution of the aluminium oxide that may be present on the S-phase.

However, the observed trenching could not be exclusively induced by cathodic driven localised corrosion and subsequent dissolution of the Al passive film. As presented in Fig. 2 (d) and (e), the pH at the cathodic zones observed on AA2024 reached 7.8 and 7.95, respectively. In fact, as the pH at the surface level may differ around 0.1–0.6 pH units [39,40] from the values measured by SIET at 50 μm, the pH at the surface in the vicinity of intermetallics might have reached nearly ~8.5 (SIET measurements were performed ~50 μm above the surface) - which is not high enough to induce relevant dissolution of the matrix.
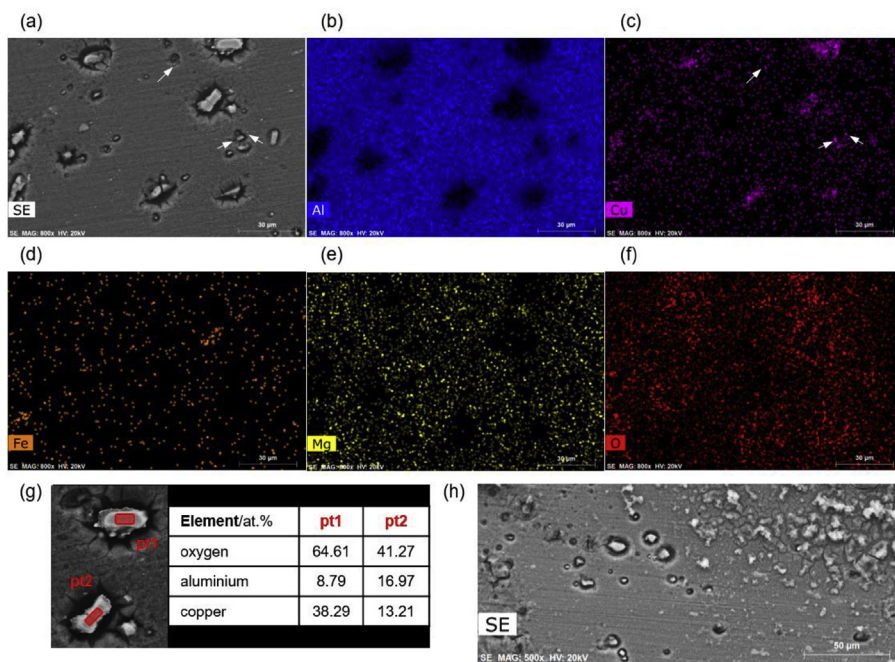

Element/at.%	pt1	pt2
oxygen	64.61	41.27
aluminium	8.79	16.97
copper	38.29	13.21

Fig. 3. (a) SEM secondary electron image from the cathodic region of AA2024 (M1) after 20 h of exposure to 12.00 mM NaCl solution. (b, c, d, e, f) Corresponding EDX elemental maps of Al, Cu, Fe, Mg and O. The white arrows in (c) Indicate Cu redistribution. (g) Inset of intermetallics from "(a)" and the corresponding chemical composition obtained by EDX from their centres (points 1 and 2). (h) secondary electron image of AA2024 presenting both cathodic (left) and anodic (right) regions.

Moreover, local EDX analysis of individual particles showed high oxygen contents together with relatively high Al contents over the Cu-rich particles (points 1 and 2 in Fig. 3(g)); indicating that the oxygen detected over (and especially around) IMPs (Fig. 3(f)) is most likely related to the build-up of corrosion products due to the anodic dissolution of the matrix triggered by the micro-galvanic couplings with the IMPs. Once again, if only cathodic attack would be responsible for the observed trenching, oxygen should not be detected close to the precipitates at such high intensities (~41 and ~65% for points 1 and 2, respectively), as stable Al oxides would not be expected (these corrosion products could not refer to hydroxychlorides, since the presence of Cl$^-$ was not relevant, being identical to values randomly monitored over the surface). Therefore, the observed trenching of the Al matrix is resulted of both chemical (cathodic attack) and electrochemical dissolution processes - in agreement with previous authors [27,31].

The limitations in the spatial resolution of SVET/SIET techniques could explain why the anodic activities on the trenched regions could not have been detected. It is well documented that the individual response of IMPs is often omitted by these local electrochemical techniques [41]. For instance, anodic reactions could take place on the S-phase even if the measured net current is only cathodic [38]. As explained by Snihirova [31], when upward positive and negative fluxes are present, only the resulting total flux is detected by SVET. At the interfaces between intermetallics and the matrix, the H$^+$ ions, generated due to Al^{3+} hydrolysis, meet the alkaline species generated at the cathode and the local pH gradients are neutralized at these frontier zones, which also indicate that the measured pH might be underestimated. A possible additional reason for the weak detection of anodic dissolution from the S-phase is that the top layers of the remnant become increasingly more porous and richer in Cu, and thus the anodic activities tend to take place progressively at deeper locations inside the sponge-like structure [23].

Considering the SIET findings and the estimations from Refs. [39,40], the pH values from the cathodic regions of the alloy were not expected to surpass ~8.5. Thus, localised corrosion processes (local breakdown of the passive film) were likely to take place on these regions, due to the presence of a chemically stable passive film at the expected pH ranges − otherwise, a more generalised corrosion behaviour would be expected as a result of a passive film chemically unstable [19]. Fig. 3(h) shows an interfacial zone between regions subjected to cathodic (left) and anodic (right) reactions that respectively presented trenching (localised corrosion) and corrosion products uniformly distributed (generalised corrosion). In agreement with Chen observations [19], as aluminium oxides are extremely soluble in acidic NaCl solutions, the corrosion of AA2024 tends to be more generalised in the acidic zones (pH of 5.2–4.5) compared to the near-neutral ones (pH of 7.15–7.5). Thus, while the cathodic zones were subjected to a combination of chemical and electrochemical dissolution mechanisms, the anodic zones were preferentially dissolved via electrochemical means.

As result of the low cathode/anode area ratio of M1, the graphite electrode was not capable of completely polarising the alloy, which acted as a mixed anode and cathode. Thereby, targeting at a complete separation of the anodic and cathodic processes between AA2024 and graphite, a model couple with lower AA2024/graphite area ratio (1.5) was also tested.

3.2. Corrosion behaviour of the M2 model couple

In the M2 model couple, a complete separation between anodic and cathodic processes could be observed (Fig. 4(a, b, c)). The current density and pH distributions were also in good agreement.

SVET and SIET maps obtained after 1 h (Fig. 4. (a) and (d)) highlighted that acidification and alkalinisation processes correlate very well to the zones displaying anodic and cathodic activities detected in the SVET maps. Despite the apparent purely anodic behaviour of AA2024 in this case, the development of reduction reactions on the alloy cannot be completely discarded, as these could be easily cancelled by the overwhelming anodic activity.

The spatial distribution of the anodic and cathodic areas remained nearly unchanged throughout all the immersion period. Some hydrogen bubbling [42] was observed at early stages, on the AA2024 surface but these bubbles disappeared after 3 h (Fig. 4 (g) and (h)) of immersion. This reaction reflects an increase in the kinetics of the hydrogen reduction induced by the low pH arising from the hydrolysis of Al^{3+} ions [43]. Simultaneously, the dealloying of S-phase could also promote an intense development of hydrogen evolution [36].

The magnitude of both anodic and cathodic current densities decreased as a function of time. The distributions of anodic and cathodic activities correlated well with local pH changes, which presented the most acidic pH values, corresponding to highest dissolution rate, approximately after 1 h of immersion. The pH over the anodic zones slightly increased along the immersion time, suggesting a decrease of Al dissolution rate. At the same time, the decrease of the cathodic activity was accompanied by a corresponding decrease of pH, from 10.05 (1 h) to 9.3 (5 h), suggesting the decrease of the oxygen reduction reaction intensity. The observed behaviour could be related to a local blockage of the alloy surface by corrosion products (Fig. 5) that may provide physical protection, slowing down the intensity of the galvanic corrosion [9]. By the end of the test (20 h), corrosion products were clearly detected being also precipitated over the epoxy, displaying a pH of ~5.2–6.8 (Fig. 4(i)).

SEM-EDX analysis (Fig. 5) shows that the AA2024 surface revealed intense anodic dissolution due to precipitation of species containing Al, Mg and, possibly, Cu outside the electrode surface, i.e. on the epoxy surface. Considering that the passive film, formed on Al, is often unstable outside the pH range from 4 to 9 [19], it could be dissolved significantly in the pH conditions established in the Al matrix over the time. The Cu-enrichment processes related to IMPs were not detected in this case, as the Cu signal appeared limited to the areas occupied by the precipitates (Fig. 6 (a) and (c)). The small amount of Cu observed outside the electrode (Fig. 5(c)) was probably a result of the matrix etching, as the alloy contains 0.2–0.5 wt% of copper in solid solution [23].

From the SEM-EDX analysis carried out on the AA2024 surface, two distinct mechanisms of corrosion can be proposed. The first one includes a generalised dissolution of the matrix, which covered an important part of the surface, leaving no evident signs of corrosion and apparently intact IMPs (Fig. 7). In fact, SEM images show that well defined IMPs were left in positive relief, while the Al matrix was consumed (Fig. 6(f)). The second mechanism involves intergranular corrosion (IGC), which seems to be associated with domes of corrosion products (Al hydroxychlorides). As shown in Fig. 6, the occurrence of IGC seemed to take place randomly on the surface and not particularly associated with Cu-rich inclusions. These observations suggest that the development of IGC in this case was not related to local galvanic couplings between IMPs and the matrix. Most probably, the grain boundaries were preferentially attacked because they are not as noble (due to Cu-depletion) as the rest of the matrix [20]. According to Suter et al. [16], initial microcraks may form being induced by hydrogen evolution and followed by acidification (which was detected by SIET on AA2024) due to hydrolysis of cations Al^{3+} formed during anodic dissolution of AA2024. Concomitantly, due to the lack of protection offered by the passive layer that was exposed to pH values around 4.7 (Fig. 4), the
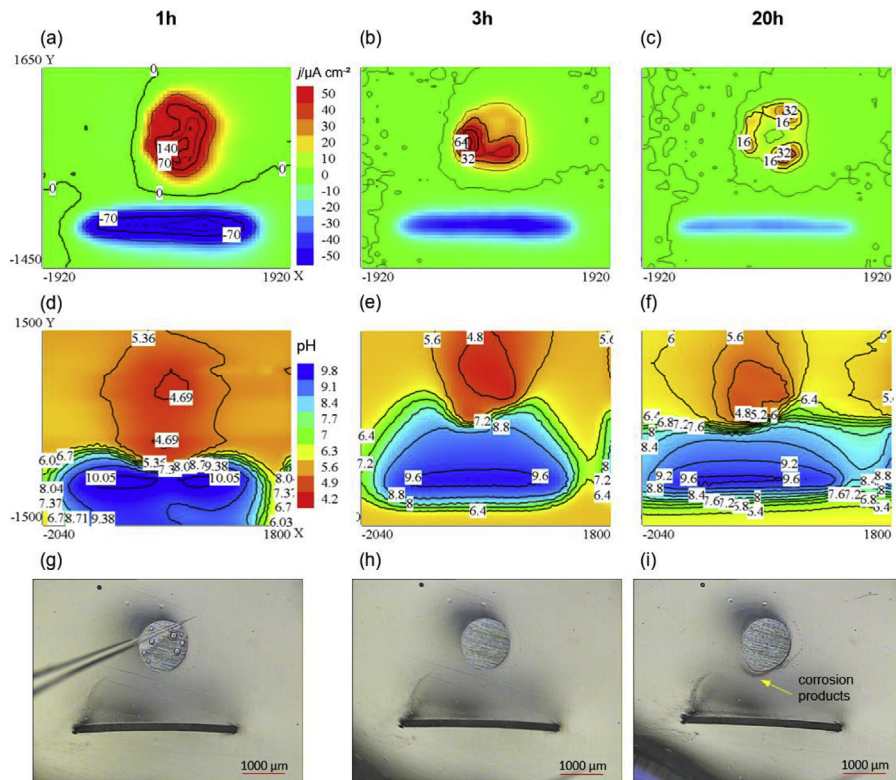
Fig. 4. (a, b, c) Current density (j / µA cm^{-2}) and (d, e, f) pH maps obtained from M2 in 12.00 mM NaCl solution after: (a, d) 1 h, (b, e) 3 h and (c) 20 h of exposure. (g, h, i) Corresponding optical micrographs taken *in situ* after the scans. X and Y coordinates represent the length of the mapping in µm. The current density and pH scales are valid for all respective j and pH maps. X and Y scales from (a) and (d) are respectively valid for the j and pH maps. Estimated potential of M2 = −390 mV $_{(Ag/AgCl)}$ (Fig. 8).
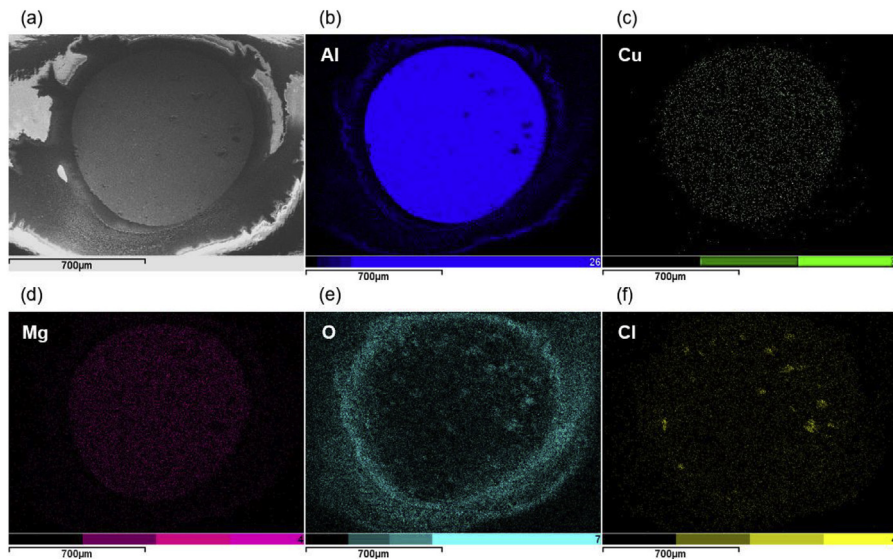
Fig. 5. (a) SEM secondary electron image of AA2024 from M2 after 20 h of exposure to 12.00 mM NaCl solution. (b, c, d, e, f) Corresponding EDX elemental maps of Al, Cu, Mg, O and Cl.

alloy started to dissolve in a generalised form in addition to the localised corrosion events [19].

From the Zhang and Frankel investigation on the anodic polarisation of AA2024-T3 [44], two breakdown potentials were observed, the more active one being related to the transient dissolution of S-phase intermetallics, while the nobler ones are associated to the growth of IGC. Similarly, Guillaumin et al. [20]

observed that the more noble breakdown potential corresponded to dissolution of matrix and grain boundaries.

3.3. Comparison between the corrosion behaviour of M1 and M2

The extent of galvanic corrosion was expected to be higher for the M2 model couple, due to the disadvantageous electrode area
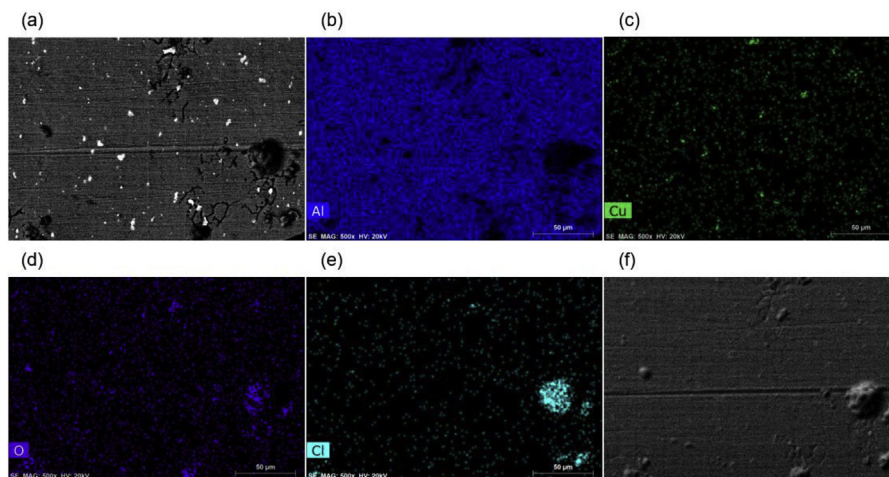
Fig. 6. (a) SEM backscattered electron image from a region of AA2024 surface (M2) presenting intergranular corrosion after 20 h in 12.00 mM NaCl electrolyte. (b, c, d, e) Corresponding EDX elemental maps of Al, Cu, O and Cl. (f) the corresponding secondary electron image with topography information.
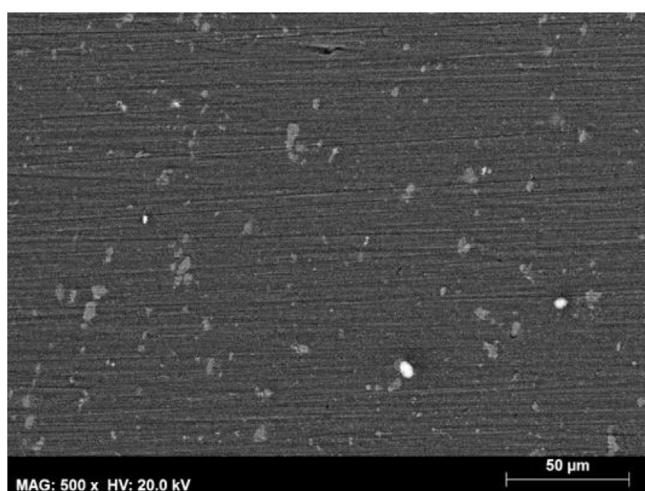

Fig. 7. SEM secondary electron image from a region of AA2024 surface (M2) subjected to generalised dissolution after 20 h of immersion in 12.00 mM NaCl electrolyte.

ratio [33]. However, the magnitude of the cathodic current densities on graphite was significantly lower compared to the results previously reported for M1. This fact suggests that micro-galvanic couples matrix/intermetallics indeed play an important role on the galvanic corrosion mechanism of M1. This suggestion is supported by the findings of Boag and Hughes [43], stating that the trenching of the matrix is a cathodically limited process, as the intermetallics can support much higher current densities compared to the equivalent matrix area. In all cases, due to a better separation between the anodic and cathodic reactions for M2, the difference between extreme values of pH was higher than in case of M1.

In a localised study carried out on AA2024-T3, Leblanc et al. [11] stated that as the area ratio of cathodic IMPs increases, the corrosion mechanism dramatically changes from the dissolution of Al_2CuMg inclusions to intense attack of the matrix. This model may help to illustrate the observed discrepancies in the corrosion mechanisms of M1 and M2. In M1 case, the graphite surface was not large enough to guarantee a complete anodic polarisation of AA2024. Therefore, the reduction of oxygen was still capable of proceeding on the alloy surface and especially on Cu-rich IMPs,

making matrix susceptible to trenching. Conversely, regarding M2, the high cathode/anode area ratio was able to induce a generalised anodic dissolution due to the likely higher overpotentials attained.

Seeking at assessing the electrochemical behaviour of AA2024 as function of applied overpotentials, the alloy was subjected to potentiodynamic polarisations tests. Fig. 8(a) shows an anodic polarisation curve of AA2024-T3 plotted with the cathodic polarisation curve of graphite obtained in 12.00 mM NaCl electrolyte. These polarisation curves are presented in total current as an attempt of estimating the overpotentials established when the alloy is galvanic coupled to graphite for the model configurations considered. Thereby, the overpotential of AA2024 was considered to be the intersection of its anodic curve with the cathodic curve of graphite for the respective models. The current values were achieved by multiplying the measured current densities by the areas of the corresponding electrodes.

Considering the alloy OCP approximately as ~ -490 mV$_{(Ag/AgCl)}$ and the galvanic potential of the models to be around -420 mV$_{(Ag/AgCl)}$ (E_{M1}) and -390 mV$_{(Ag/AgCl)}$ (E_{M2}), the overpotential of the alloy was estimated as $+70$ mV and $+100$ mV respectively for M1 and M2. This difference in the overpotential of AA2024 depending on the alloy/graphite area ratio might thus explain the different corrosion mechanisms observed for the alloy. Using the nomenclature employed by Zhang et al. [44], it can be seen that E_{M1} is nearly coincident to the breakdown potential referred as E_1, which is assigned to pitting corrosion/S-phase dissolution (Fig. 8(c)). Similarly, E_{M2} might be correlated to the potential referred as E_2, which is related to the initiation and growth of IGC (Fig. 8(b)). For instance, the anodic polarisation curve of AA2024 here achieved is quite similar to that obtained by Zhang [44] in 1 M NaCl, as both were obtained at the same scan rate and exposing the same area of the alloy (ground surface state).

From Zhang et al. results [44], a critical potential E_c representing the transition between pitting and IGC is clearly depicted. In the present case however, only slight signals of the transition potential could be observed, namely, a small current peak located at potentials immediately below E_2. This absence of a clearly detectable transition might arise from the fact that curves of Fig. 8(a) were recorded under aerated conditions, while Zhang obtained their curve working in Ar-deaerated media. Indeed, the presence of oxygen might have induced an acceleration of corrosion processes, which could explain the quite limited potential range comprising the development of both types of corrosion here verified.
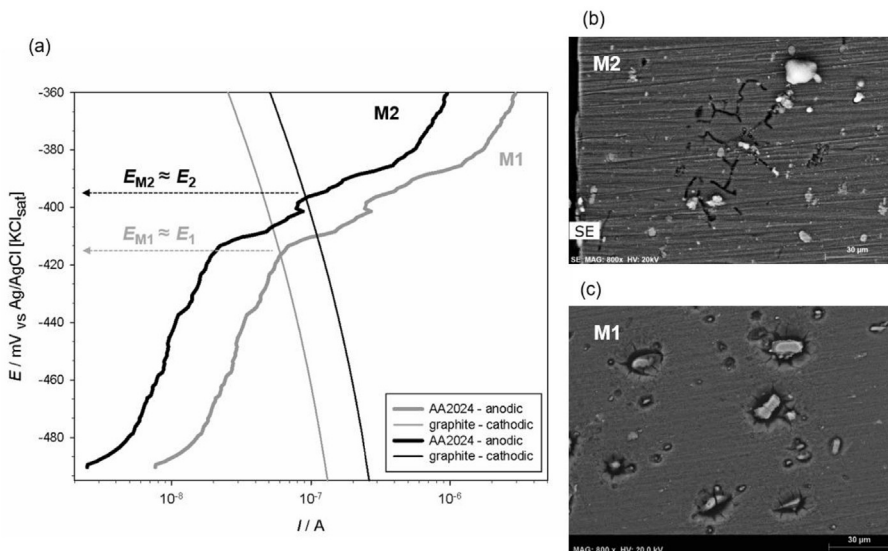
Fig. 8. (a) Intersections of the anodic polarisation curves for AA2024-T3 and the cathodic polarisation curves for graphite simulating the galvanic coupling of M1 and M2 in 12.00 mM NaCl medium. These polarisation curves are expressed in µA (current I). AA2024-T3 surfaces from (b) M2 and (c) M1 respectively presenting IGC and trenching after 20 h of exposure to 12.00 mM NaCl.

In accordance with the outcomes of Zhang et Frankel [44], at the potential E_{M2}, the transient dissolution of S-phase should occur quite fast, which may explain the initial bubbles formation in this case. Furthermore, such a high overpotential could also explain why redeposition of Cu was not verified around intermetallics in the M2 case: although the dissolution of Cu from the matrix was promoted, the E_{M2} potential was too high to allow for Cu redeposition. As detailed by Blanc et al. [45,46], the optimum potential for deposition of Cu is actually not far from E_1 (closer to the OCP). It is also worth mentioning that pitting corrosion was not observed in the M2 case. Very few holes were found, but likely to be associated with the IGC cracks and detachment of intermetallics. For instance, at high potentials, while initiated IGC could grow, pits are likely to be repassivated, once the current density has already reached a maximum at E_c [44]. Although the overpotentials introduced by coupling with graphite might be compared to the critical potentials from the potentiodynamic polarisation curves (Fig. 8), helping to illustrate the corrosion mechanisms of the models, such comparisons remain a simplification of the actual galvanic processes.

The analogy of the different corrosion mechanisms obtained, depending on the alloy/graphite area ratio, with the anodic polarisation curve of AA2024-T3 considers the graphite as a counter electrode, which provides an active surface for the ORR to occur. Despite the fact that graphite is a quite inert material, the presence of superficial microcracks was eventually assigned to the graphite foil at long immersion times (beyond 20 h). Chloride ions were reported as being able to intercalate between the graphite layers, thus, causing exfoliation of the material [47]. For instance, small contents of Na and Cl were detected after exposing the M2 sample for 20 h to the NaCl solution (Fig. 9), while post-immersion rinsing was supposed to remove them at a great extent. The influence of this degradation phenomenon on the corrosion mechanisms of the galvanic pairs was not considered here and might be the focus of future studies.

A diagram presenting the activity of different species vs pH related to the corrosion of AA2024 (Fig. 10(a)) was constructed using the Medusa Software [26,48]. From this diagram based on thermodynamic data, it is possible to correlate the nature of the corrosion products with the local pH values measured by SIET. For instance, $Al(OH)_3$ is expected to be the most stable phase at the pH range of ~4–11 for the concentration of species here considered ($[Al^{3+}] = 5 \times 10^{-3}$ M, $[Mg^{2+}] = [Cu^{2+}] = 2.5 \times 10^{-3}$ M, $[Na^+] = [Cl^-] = 12 \times 10^{-3}$ M and $[CO^{2-}_3] = 5 \times 10^{-5}$ M). $[Na^+]$ and $[Cl^-]$ were chosen as corresponding to the electrolyte concentration; $[CO^{2-}_3]$ was due the expected ambient conditions; $[Al^{3+}]$ was based on the calculations for a model Al-Cu [49] and adopted according to the present experimental setup; $[Mg^{2+}]$ and $[Cu^{2+}]$ were chosen as extreme approximation for the case of S-phase dissolution after confirmation by SEM/EDX analysis that Mg and Cu were dissolved during the corrosion process.

In the M1 case, the $Al(OH)_3$ phase could be assigned to both anodic (pH of 5.2–4.5) and cathodic zones (pH of 7.1–7.5) of the alloy. Moreover, in the cathodic zones, CuO might also have been formed, as this phase is stable over the referred pH range. In this case, one might expect that the Cu redeposition process associated with the cathodic intermetallics (Fig. 3 (c) and (g)) could be related to the precipitation of CuO — and not only to the deposition of metallic Cu, as often presented in the literature [10,19,22,23].

As the spatial resolution of the local EDX performed on the Cu-rich IMPs was not sufficiently high to clearly assign the CuO phase (Fig. 3), a physical Al/Cu galvanic couple model was built (electrodes diameter = 2 mm, cathode/anode area ratio = 1) to simulate the galvanic coupling between the Cu-rich precipitates and the Al matrix [50,51]. The Al/Cu model was tested in 6.00 mM $CuCl_2$ solution in order to verify if the precipitation of CuO could occur when Cu^{2+} ions are present. Fig. 10(b) shows the surface of the Cu electrode after 30 min of immersion and the corresponding results of SEM-EDX analysis. By comparing the secondary electron image with the EDX elemental mapping of O, it can be seen that the precipitates formed are quite rich in oxygen (55.01 ± 4.53 at.%). Thus, these are likely to be mainly composed of copper oxides (Cl was only detected at small amount (2.39 ± 0.70 at.%)) and, most likely, of CuO - taking into consideration the black colour of the phase.

Concerning the M2 sample, according to the diagram (Fig. 10(a)), $Al(OH)_3$ was preferentially formed around the alloy, far from its centre, while the precipitation of $Al(OH)_2Cl$ was likely to occur on its central regions, where pH reached ~4.7 (at ~50 µm from the
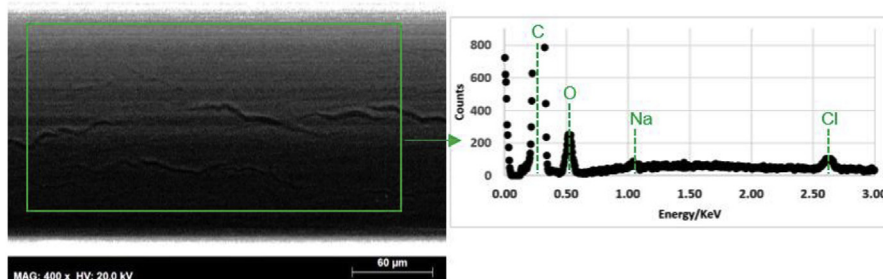
Fig. 9. SEM secondary electron image of the graphite surface (M2) after 20 h of immersion in 12.00 mM solution and the corresponding local EDX spectra.
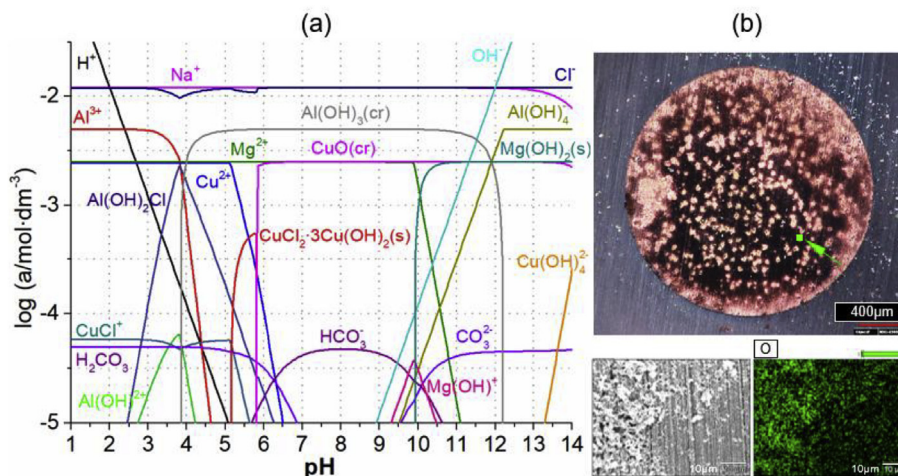

Fig. 10. (a) Logarithm of activity of the species in solution as a function of pH for AA2024 dissolution at average ionic strength 0.05 M. Corrected values of K were used for the following reactions $5Zn^{2+} + 2Cl^- + 8H_2O = 8H^+ + Zn_5(OH)_8Cl_2$ (log K = −34.5) and $5Zn^{2+} + 6H_2O + 2CO_3^{2-} = 6H^+ + Zn_5(OH)_6(CO_3)_2$ (log K = −5.4), instead of the ones used by Medusa software [48]. Corresponding stability constants were found in Ref. [52]. Additionally to the complexes existing in the database, Al hydroxychlorides $Al(OH)Cl^+$ and $Al(OH)_2Cl$ complexes were added to the Hydra-Medusa database [26]. (b) Cu surface of the Al/Cu galvanic couple model after 30 min of exposure to 6.00 mM $CuCl_2$ solution and the corresponding SEM-EDX analysis (secondary electron image and elemental map of O) from the indicated point.

surface). Considering that the pH might have reached ~4.1 at the surface level [39,40], the precipitation of Al hydroxychlorides would be expected along with the generation of soluble Al^{3+} ions — which could explain the observed generalised dissolution of AA2024. These predictions are in accordance with the EDX elemental maps of Al, O and Cl presented in Fig. 5. Finally, the pH (~5.2−6.8) at the epoxy surface where corrosion products were observed *in situ* (Fig. 4(i)) corresponds to the stability zone of $Al(OH)_3$ and partially to that of CuO.

4. Conclusions

The quasi-simultaneous SVET/SIET studies revealed important information to discriminate two different mechanisms governing the corrosion processes of two AA2024-T3/graphite model galvanic couples with different area ratio of the coupled materials. Moreover, SEM-EDX analysis provided relevant data to unveil important features of the corrosion mechanisms of the two model couples, made with AA2024/graphite ratio of 10 (M1) or 1.5 (M2).

Concerning the M1 model couple (AA2024/graphite ratio = 10), the graphite electrode was not able to anodically polarise the entire surface of AA2024, giving rise to the establishment of ORR within Cu-rich IMPs (including Cu remnants of the dealloyed S-phase). Trenching of the Al matrix around precipitates was assigned to the cathodic/alkaline zones, while generalised corrosion was detected on the anodic/acidic zones. The observed trenching process appears

to be the result of both chemical (alkaline attack) and electrochemical dissolution processes. Local pH alkalinisation, associated with the trenched particles, was not high enough to promote a complete dissolution of the passive layer. Since high amounts of oxygen were detected by EDX close to the trenches, it is possible to assume that anodic dissolution of the matrix also occurred, despite the fact that no anodic activity related to trenching could be detected by SVET/SIET, mainly, due to resolution limitations.

Regarding the M2 model (AA2024/graphite ratio = 1.5), a complete separation between the anodic and cathodic processes was clearly evidenced. In this case, the alloy was subjected to a generalised dissolution process, since the Al passive film was not stable at the pH values found (<4.7). Moreover, a second type of corrosion took place – intergranular corrosion. This corrosion form did not follow the spatial distribution of precipitates, suggesting that the corrosion of the grain boundaries was not influenced by the cathodic nature of the intermetallics. Al hydroxychlorides were the only phases often associated with the cracks of IGC. Furthermore, no trenching was detected in this case.

The effect of changing the electrodes area ratio on the corrosion mechanism of AA2024 was compared to the effect of polarising the alloy at different potentials. The trenching process observed for M1 was assigned to the more active breakdown potential of the curve, while the generalised dissolution (matrix and grain boundaries) verified for M2 was referred to the more noble breakdown potential.

Acknowledgements

References

[1] R. Srinivasan, L.H. Hihara, Utilization of hydrophobic coatings on insulative skirts to attenuate galvanic corrosion between mechanically-fastened aluminum alloy and carbon-fiber reinforced polymer-matrix composites, Electrochem. Commun. 72 (2016) 96–99, https://doi.org/10.1016/j.elecom.2016.09.014.

[2] Z. Liu, M. Curioni, P. Jamshidi, A. Walker, P. Prengnell, G.E. Thompson, P. Skeldon, Electrochemical characteristics of a carbon fibre composite and the associated galvanic effects with aluminium alloys, Appl. Surf. Sci. 314 (2014) 233–240, https://doi.org/10.1016/j.apsusc.2014.06.072.

[3] R. Srinivasan, J.A. Nelson, L.H. Hihara, Development of guidelines to attenuate galvanic corrosion between mechanically-coupled aluminum and carbon-fiber reinforced epoxy composites using insulation layers, J. Electrochem. Soc. 162 (2015) C545–C554, https://doi.org/10.1149/2.0611510jes.

[4] F. Bellucci, A. Di Martino, C. Liberti, Electrochemical behaviour of graphite-epoxy composite materials (GECM) in aqueous salt solutions, J. Appl. Electrochem. 16 (1986) 15–22, https://doi.org/10.1007/BF01015979.

[5] S. Palani, T. Hack, J. Deconinck, H. Lohner, Validation of predictive model for galvanic corrosion under thin electrolyte layers: an application to aluminium 2024-CFRP material combination, Corros. Sci. 78 (2014) 89–100, https://doi.org/10.1016/j.corsci.2013.09.003.

[6] Boeing, Boeing 787 from the Ground Up, AEROMAGAZINE. (n.d.). http://www.boeing.com/commercial/aeromagazine/articles/qtr_4_06/article_04_2.html (accessed November 3, 2017).

[7] S. Payan, Y. Le Petitcorps, J.-M. Olive, H. Saadaoui, Experimental procedure to analyse the corrosion mechanisms at the carbon/aluminium interface in composite materials, Compos. Part A Appl. Sci. Manuf. 32 (2001) 585–589, https://doi.org/10.1016/S1359-835X(00)00126-3.

[8] M. Serdechnova, S. Kallip, M.G.S. Ferreira, M.L. Zheludkevich, Active self-healing coating for galvanically coupled multi-material assemblies, Electrochem. Commun. 41 (2014) 51–54, https://doi.org/10.1016/j.elecom.2014.01.023.

[9] E. Håkansson, J. Hoffman, P. Predecki, M. Kumosa, The role of corrosion product deposition in galvanic corrosion of aluminum/carbon systems, Corros. Sci. 114 (2017) 10–16, https://doi.org/10.1016/j.corsci.2016.10.011.

[10] R.G. Buchheit, Local dissolution phenomena Associated with S Phase (Al2CuMg) particles in aluminum alloy 2024-T3, J. Electrochem. Soc. 144 (1997) 2621, https://doi.org/10.1149/1.1837874.

[11] P. Leblanc, G.S. Frankel, A study of corrosion and pitting initiation of AA2024-T3 using atomic force microscopy, J. Electrochem. Soc. 149 (2002) B239, https://doi.org/10.1149/1.1471546.

[12] J.B. Jorcin, C. Blanc, N. Pébère, B. Tribollet, V. Vivier, Galvanic coupling between pure copper and pure aluminum, J. Electrochem. Soc. 155 (2008) C46, https://doi.org/10.1149/1.2803506.

[13] N. Birbilis, R.G. Buchheit, Electrochemical characteristics of intermetallic phases in aluminum alloys an experimental survey and discussion, J. Electrochem. Soc. 152 (2005) B140–B151, https://doi.org/10.1149/1.1869984.

[14] A.E. Hughes, R. Parvizi, M. Forsyth, Microstructure and corrosion of AA2024, Corros. Rev. 33 (2015) 1–30, https://doi.org/10.1515/corrrev-2014-0039.

[15] D. Zhu, W.J. van Ooij, Corrosion protection of AA 2024-T3 by bis-[3-(triethoxysilyl)propyl]tetrasulfide in neutral sodium chloride solution. Part 1: corrosion of AA 2024-T3, Corros. Sci. 45 (2003) 2163–2175, https://doi.org/10.1016/S0010-938X(03)00060-X.

[16] T. Suter, R.C. Alkire, Microelectrochemical studies of pit initiation at single inclusions in Al 2024-T3, J. Electrochem. Soc. 148 (2001) B36, https://doi.org/10.1149/1.1344530.

[17] L. Lacroix, L. Ressier, C. Blanc, G. Mankowski, Combination of AFM, SKPFM, and SIMS to study the corrosion behavior of S-phase particles in AA2024-T351, J. Electrochem. Soc. 155 (2008) C131–C137, https://doi.org/10.1149/1.2833315.

[18] L. Lacroix, L. Ressier, C. Blanc, G. Mankowski, Statistical study of the corrosion behavior of Al2CuMg intermetallics in AA2024-T351 by SKPFM, J. Electrochem. Soc. 155 (2008) C8, https://doi.org/10.1149/1.2799089.

[19] G.S. Chen, M. Gao, R.P. Wei, Microconstituent-induced pitting corrosion in aluminum alloy 2024-T3, Corrosion 52 (1996) 8–15, https://doi.org/10.5006/1.3292099.

[20] V. Guillaumin, G. Mankowski, Localized corrosion of 2024 T351 aluminium alloy in chloride media, Corros. Sci. 41 (1998) 421–438, https://doi.org/10.1016/S0010-938X(98)00116-4.

[21] A. Boag, A.E. Hughes, A.M. Glenn, T.H. Muster, D. McCulloch, Corrosion of AA2024-T3 Part I: localised corrosion of isolated IM particles, Corros. Sci. 53 (2011) 17–26, https://doi.org/10.1016/j.corsci.2010.09.009.

[22] W. Qafsaoui, M.W. Kendig, H. Perrot, T. Takenouti, Effect of 1-pyrrolidine dithiocarbamate on the galvanic coupling resistance of intermetallics - aluminum matrix during corrosion of AA 2024-T3 in a dilute NaCl, Corros. Sci. 92 (2015) 245–255, https://doi.org/10.1016/j.corsci.2014.12.011.

[23] M.B. Vukmirovic, N. Dimitrov, K. Sieradzki, Dealloying and corrosion of Al alloy 2024-T3, J. Electrochem. Soc. 149 (2002) B428, https://doi.org/10.1149/1.1498258.

[24] S.V. Lamaka, M. Taryba, M.F. Montemor, H.S. Isaacs, M.G.S. Ferreira, Quasi-simultaneous measurements of ionic currents by vibrating probe and pH distribution by ion-selective microelectrode, Electrochem. Commun. 13 (2011) 20–23, https://doi.org/10.1016/j.elecom.2010.11.002.

[25] M. Taryba, S.V. Lamaka, D. Snihirova, M.G.S. Ferreira, M.F. Montemor, W.K. Wijting, S. Toews, G. Grundmeier, The combined use of scanning vibrating electrode technique and micro-potentiometry to assess the self-repair processes in defects on "smart" coatings applied to galvanized steel, Electrochim. Acta 56 (2011) 4475–4488, https://doi.org/10.1016/j.electacta.2011.02.048.

[26] A. Alvarez-Pampliega, S.V. Lamaka, M.G. Taryba, M. Madani, J. De Strycker, E. Tourwé, M.G.S. Ferreira, H. Terryn, Cut-edge corrosion study on painted aluminum rich metallic coated steel by scanning vibrating electrode and micro-potentiometric techniques, Electrochim. Acta 61 (2012) 107–117, https://doi.org/10.1016/j.electacta.2011.11.110.

[27] H. Shi, Z. Tian, T. Hu, F. Liu, E.H. Han, M. Taryba, S.V. Lamaka, Simulating corrosion of Al2CuMg phase by measuring ionic currents, chloride concentration and pH, Corros. Sci. 88 (2014) 178–186, https://doi.org/10.1016/j.corsci.2014.07.021.

[28] M.G. Taryba, M.F. Montemor, S.V. Lamaka, Quasi-simultaneous mapping of local current density, pH and dissolved O 2, Electroanalysis 27 (2015) 2725–2730, https://doi.org/10.1002/elan.201500286.

[29] H. Shi, E.-H. Han, F. Liu, T. Wei, Z. Zhu, D. Xu, Study of corrosion inhibition of coupled Al2Cu–Al and Al3Fe–Al by cerium cinnamate using scanning vibrating electrode technique and scanning ion-selective electrode technique, Corros. Sci. 98 (2015) 150–162, https://doi.org/10.1016/j.corsci.2015.05.019.

[30] S. Wang, H. Ming, J. Ding, Z. Zhang, J. Wang, E.H. Han, A. Atrens, Effect of H3BO3 on corrosion in 0.01 M NaCl solution of the interface between low alloy steel A508 and alloy 52 M, Corros. Sci. 102 (2016) 469–483, https://doi.org/10.1016/j.corsci.2015.10.040.

[31] D. Snihirova, M. Taryba, S.V. Lamaka, M.F. Montemor, Corrosion inhibition synergies on a model Al-Cu-Mg sample studied by localized scanning electrochemical techniques, Corros. Sci. 112 (2016) 408–417, https://doi.org/10.1016/j.corsci.2016.08.008.

[32] F. Bellucci, Galvanic corrosion between nonmetallic composites and metals II. Effect of area ratio and environmental degradation, Corrosion 48 (1992) 281–291, https://doi.org/10.5006/1.3315934.

[33] F. Bellucci, Galvanic corrosion between nonmetallic composites and metals:I effect of metal and of temperature, Corrosion 47 (1991) 808–819, https://doi.org/10.5006/1.3585192.

[34] L.B. Coelho, M.-G. Olivier, The inhibition efficiency of different species on AA2024/graphite galvanic coupling models depicted by SVET, Corros. Sci. 136 (2018) 292–303, https://doi.org/10.1016/j.corsci.2018.03.015.

[35] F. Eckermann, T. Suter, P.J. Uggowitzer, A. Afseth, P. Schmutz, The influence of MgSi particle reactivity and dissolution processes on corrosion in Al-Mg-Si alloys, Electrochim. Acta 54 (2008) 844–855, https://doi.org/10.1016/j.electacta.2008.05.078.

[36] L. Paussa, F. Andreatta, D. De Felicis, E. Bemporad, L. Fedrizzi, Investigation of AA2024-T3 surfaces modified by cerium compounds: a localized approach, Corros. Sci. 78 (2014) 215–222, https://doi.org/10.1016/j.corsci.2013.10.001.

[37] Y.L. Cheng, Z. Zhang, F.H. Cao, J.F. Li, J.Q. Zhang, J.M. Wang, C.N. Cao, A study of the corrosion of aluminum alloy 2024-T3 under thin electrolyte layers, Corros. Sci. 46 (2004) 1649–1667, https://doi.org/10.1016/j.corsci.2003.10.005.

[38] M. Iannuzzi, J. Kovac, G.S. Frankel, A study of the mechanisms of corrosion inhibition of AA2024-T3 by vanadates using the split cell technique, Electrochim. Acta 52 (2007) 4032–4042, https://doi.org/10.1016/j.electacta.2006.11.019.

[39] O. Dolgikh, A. Demeter, S.V. Lamaka, M. Taryba, A.C. Bastos, M.C. Quevedo, J. Deconinck, Simulation of the role of vibration on Scanning Vibrating Electrode Technique measurements close to a disc in plane, Electrochim. Acta 203 (2016) 379–387, https://doi.org/10.1016/j.electacta.2016.01.188.

[40] M. Taryba, S. Lamaka, M.G.S. Ferreira, pH-measurements on a steel coating interface with microelectrode, in: Eur. Corros. Congr. Eurocorr 2012, Istanbul, 2012.

[41] G. Williams, A.J. Coleman, H.N. McMurray, Inhibition of Aluminium Alloy AA2024-T3 pitting corrosion by copper complexing compounds, Electrochim. Acta 55 (2010) 5947–5958, https://doi.org/10.1016/j.electacta.2010.05.049.

[42] K.A. Yasakau, M.L. Zheludkevich, S.V. Lamaka, M.G.S. Ferreira, Mechanism of corrosion inhibition of AA2024 by rare-earth compounds, J. Phys. Chem. B 110 (2006) 5515–5528, https://doi.org/10.1021/jp0560664.

[43] A. Boag, R.J. Taylor, T.H. Muster, N. Goodman, D. McCulloch, C. Ryan, B. Rout, D. Jamieson, A.E. Hughes, Stable pit formation on AA2024-T3 in a NaCl

environment, Corros. Sci. 52 (2010) 90—103, https://doi.org/10.1016/j.corsci.2009.08.043.

[44] W. Zhang, G.S. Frankel, Transitions between pitting and intergranular corrosion in AA2024, Electrochim. Acta 48 (2003) 1193—1210, https://doi.org/10.1016/S0013-4686(02)00828-9.

[45] C. Blanc, B. Lavelle, G. Mankowski, The role of precipitates enriched with copper on the susceptibility to pitting corrosion of the 2024 aluminium alloy, Corros. Sci. 39 (1997) 495—510, https://doi.org/10.1016/S0010-938X(97)86099-4.

[46] C. Blanc, S. Gastaud, G. Mankowski, Mechanistic studies of the corrosion of 2024 aluminum alloy in nitrate solutions, J. Electrochem. Soc. 150 (2003) B396, https://doi.org/10.1149/1.1590327.

[47] S.B. Lyon, Degradation of carbon and graphite, in: Shreir's Corros, Elsevier, 2010, pp. 2271—2281, https://doi.org/10.1016/B978-044452787-5.00111-6.

[48] I. Puigdomenech, Program MEDUSA (Make Equilibrium Diagrams Using Sophisticated Algorithms), 2016. https://sites.google.com/site/chemdiagr/.

[49] D. Snihirova, S.V. Lamaka, M. Taryba, A.N. Salak, S. Kallip, M.L. Zheludkevich, M.G.S. Ferreira, M.F. Montemor, Hydroxyapatite microparticles as feedback-active reservoirs of corrosion inhibitors, ACS Appl. Mater. Interfaces 2 (2010) 3011—3022, https://doi.org/10.1021/am1005942.

[50] L.B. Coelho, M. Mouanga, M.-E. Druart, I. Recloux, D. Cossement, M.-G. Olivier, A SVET study of the inhibitive effects of benzotriazole and cerium chloride solely and combined on an aluminium/copper galvanic coupling model, Corros. Sci. 110 (2016) 143—156, https://doi.org/10.1016/j.corsci.2016.04.036.

[51] L.B. Coelho, D. Cossement, M.-G. Olivier, Benzotriazole and cerium chloride as corrosion inhibitors for AA2024-T3: an EIS investigation supported by SVET and ToF-SIMS analysis, Corros. Sci. 130 (2018) 177—189, https://doi.org/10.1016/j.corsci.2017.11.004.

[52] A. Alvarez-Pampliega, M.G. Taryba, K. Van Den Bergh, J. De Strycker, S.V. Lamaka, H. Terryn, Study of local Na+ and Cl- distributions during the cut-edge corrosion of aluminum rich metal-coated steel by scanning vibrating electrode and micro-potentiometric techniques, Electrochim. Acta 102 (2013) 319—327, https://doi.org/10.1016/j.electacta.2013.03.186.